PCCP

PAPER

View Article Online
View Journal | View Issue

Cite this: *Phys. Chem. Chem. Phys.*, 2014, **16**, 24954

Unimolecular reaction chemistry of a charge-tagged beta-hydroxyperoxyl radical†

Sui So,[a] Benjamin B. Kirk,‡[bc] Adam J. Trevitt,[bc] Uta Wille,[cd] Stephen J. Blanksby[bce] and Gabriel da Silva*[a]

Received 8th July 2014,
Accepted 9th October 2014

DOI: 10.1039/c4cp02981j

www.rsc.org/pccp

β-Hydroxyperoxyl radicals are formed during atmospheric oxidation of unsaturated volatile organic compounds such as isoprene. They are intermediates in the combustion of alcohols. In these environments the unimolecular isomerization and decomposition of β-hydroxyperoxyl radicals may be of importance, either through chemical or thermal activation. We have used ion-trap mass spectrometry to generate the distonic charge-tagged β-hydroxyalkyl radical anion, $^{\bullet}CH_2C(OH)(CH_3)CH_2C(O)O^-$, and investigated its subsequent reaction with O_2 in the gas phase under conditions that are devoid of complicating radical–radical reactions. Quantum chemical calculations and master equation/RRKM theory modeling are used to rationalize the results and discern a reaction mechanism. Reaction is found to proceed *via* initial hydrogen abstraction from the γ-methylene group and from the β-hydroxyl group, with both reaction channels eventually forming isobaric product ions due to loss of either $^{\bullet}OH$ + HCHO or $^{\bullet}OH$ + CO_2. Isotope labeling studies confirm that a 1,5-hydrogen shift from the β-hydroxyl functionality results in a hydroperoxyalkoxyl radical intermediate that can undergo further unimolecular dissociations. Furthermore, this study confirms that the facile decomposition of β-hydroxyperoxyl radicals can yield $^{\bullet}OH$ in the gas phase.

Introduction

β-Hydroxyperoxyl radicals containing the $>C(O_2^{\bullet})\text{–}C(OH)<$ moiety are oxidation intermediates of unsaturated volatile organic compounds (VOCs) in the atmosphere, where they are formed by sequential addition of the hydroxyl radical ($^{\bullet}OH$) and O_2 to a carbon–carbon double bond. During combustion of ethanol and larger alcohol fuels β-hydroxyperoxyl radicals can also form *via* hydrogen atom loss (abstraction or bond homolysis) followed by subsequent O_2 addition. β-Hydroxyperoxyl radicals will be consumed by competing bimolecular and unimolecular reactions in the atmosphere and in combustion environments.

Isoprene is the second most emitted VOC to the atmosphere, following methane, and it is the most emitted biogenic VOC. Isoprene, along with its primary oxidation products methacrolein (MACR) and methyl vinyl ketone (MVK),[1–3] possess sites of unsaturation that allow for the formation of β-hydroxyperoxyl radicals. The chemistry of β-hydroxyperoxyl radicals thus plays a key role in understanding and modeling the composition of the atmosphere. Isoprene photooxidation particularly dominates the chemistry in the forested planetary boundary layer where isoprene emissions are concentrated. Here, the photochemical oxidation of isoprene is critical to determining ozone and aerosol formation,[4–6] HO_x radical ($^{\bullet}OH + HO_2^{\bullet}$) levels and the rate of $^{\bullet}OH$ consumption (*i.e.*, $^{\bullet}OH$ reactivity).[7]

Over the last decade, field campaigns conducted over remote forested environments, which are characterized by large isoprene emission sources and relatively low levels of NO_x ($NO^{\bullet}$ + $NO_2^{\bullet}$), have reported higher-than-predicted $^{\bullet}OH$ concentrations (*ca.* 10^7 molecule cm^{-3} or 0.4 ppt) along with high $HO_2^{\bullet}:{}^{\bullet}OH$ ratios (*ca.* 100).[8] It has recently emerged that isoprene derived β-hydroxyperoxyl radicals can undergo unimolecular decomposition to replenish $^{\bullet}OH$.[9,10] These reactions have been proposed as contributors to elevated oxidative capacities in remote forested regions of the troposphere.[9] However, there has been relatively little experimental work on the unimolecular chemistry of β-hydroxyperoxyl radicals.

---

[a] *Department of Chemical and Biomolecular Engineering, The University of Melbourne, VIC 3010, Australia. E-mail: gdasilva@unimelb.edu.au*
[b] *School of Chemistry, University of Wollongong, NSW 2522, Australia*
[c] *ARC Centre of Excellence for Free Radical Chemistry and Biotechnology, Hosted by The University of Melbourne, Victoria 3010, Australia*
[d] *School of Chemistry and Bio21 Institute, The University of Melbourne, VIC 3010, Australia*
[e] *Central Analytical Research Facility, Institute for Future Environments, Queensland University of Technology, QLD 4001, Australia*

† Electronic supplementary information (ESI) available: Mass spectrometry of the photodissociation and collision induced dissociation to produce the target radical anion. Master equation simulation with and without pre-reaction complex using M06-2X and G3SX barrier heights at 307 K and 2.5 mTorr He. Optimized geometries, vibrational frequencies and moments of inertia of the wells and transition states at M06-2X level of theory. Reaction schemes of the isotope labeling experiments. See DOI: 10.1039/c4cp02981j

‡ Present address: Chemical Sciences Division, Lawrence Berkeley National Laboratory, Berkeley, CA 94720, USA.

The current study utilizes ion-trap mass spectrometry to investigate the reaction of a model distonic β-hydroxyalkyl radical anion with O_2, and probe the unimolecular reaction chemistry of the resultant β-hydroxyperoxyl radical. Quantum chemical calculations and master equation kinetic modeling are performed to gather insight into the reaction dynamics. This distonic radical ion approach to studying peroxyl radical chemistry has recently proven useful in the investigation of peroxyl radical reactions relevant to combustion, biochemistry, and atmospheric science.[11–16] It allows for definitive assignment of the mass of reaction products while avoiding complicating peroxyl radical cross and self-reactions.

Methods

Experiments

Mass spectrometry. The precursor compound, 3-hydroxy-3-methylglutaric acid was obtained from Sigma Aldrich (Castle Hill, NSW) and was used as received. Isotopically labeled oxygen $^{18}O_2$ (95%) was obtained from Cambridge Isotope Laboratories (Andover, MA). Methanol (HPLC grade) and ammonia solution (28%, AR grade) were obtained from Ajax (Sydney, Australia). Methanolic solutions of the precursor compound were adjusted to high pH using aqueous ammonia and infused *via* negative ion electrospray ionization at a rate of 5–10 μL min^{-1} into a modified Thermo Fisher Scientific LTQ (San Jose, CA) linear ion-trap mass spectrometer fitted with an IonMax electrospray ionization source. Deuterium exchange was conducted using D_1-methanol from Sigma Aldrich (Castle Hill, NSW). The modifications to this instrument to allow both photodissociation and ion–molecule experiments have been detailed previously.[17,18] A brief overview is provided below.

Photodissociation. A 2.75 inch quartz viewport is attached with a CF flange to the back plate of the ion-trap mass spectrometer to allow transmission of 266 nm radiation generated by a flash lamp-pumped Nd:YAG laser (Minilite II, Continuum, Santa Clara, CA, about 2 mJ per pulse) through the ion-trapping region of the mass spectrometer. During each MS cycle, the flash lamp is triggered by a TTL pulse generated by the mass spectrometer at the beginning of the selected MS^n activation step. In the selected MS^n step, the activation energy is set to zero to ensure no additional activation energy is supplied to the ions. Thus, the product ions generated by the laser pulse are easily identifiable. The modifications to the instruments are similar to those previously described.[19,20]

Ion–molecule reactions. During ion–molecule experiments, neutral reagents are entrained in a flow of ultra-high purity helium buffer gas (3–5 psi) through a heated septum inlet, with a syringe pump controlling the concentration of the neutral reagent. The helium/neutral flow is adjusted *via* a variable leak valve to afford a pressure in the ion-trap of 2.5 mTorr of helium.

Reaction rates for formation of the peroxyl radical anions were determined without additional neutral reagents added to the helium buffer gas. Instead, the ion-trapping region contains a small quantity of O_2 due to transmission from the atmospheric pressure ionization source. The concentration of O_2 throughout these experiments was determined by a calibration reaction (3-carboxylatoadamantyl + O_2) to be $(3.1 \pm 0.1) \times 10^9$ molecules cm^{-3}.[18] Reaction times between 30–10 000 ms are set using the activation time parameter within the Xcalibur instrument control software (Thermo Fisher Scientific, San Jose CA) with the excitation energy set at zero (arbitrary units). All spectra presented are the average of at least 50 scans.

The reaction efficiency can be calculated by first plotting the natural logarithm of the precursor ion concentration at different reaction times ($[R]_t$) relative to the initial concentration ($[R]_0$). This gives a straight line where the slope equals the pseudo first-order rate coefficient (k_1), which is illustrated in eqn (1). With a measured O_2 concentration, the second-order rate coefficient (k_2) can be obtained by eqn (2). Finally, by calculating the collision rate coefficient (k_{coll}) using the trajectory collision rate theory, the reaction efficiency (ϕ) can be determined using eqn (3).

$$\ln\frac{[R]_t}{[R]_0} = -k_1 + c \tag{1}$$

$$k_2 = \frac{k_1}{[O_2]} \tag{2}$$

$$\phi = \frac{k_2}{k_{\text{coll}}} \tag{3}$$

Statistical errors in rate measurements are typically $2\sigma < 10\%$ where σ is the standard deviation obtained from the least squares fit to the pseudo-first order decay. Systematic errors arise due to uncertainty in the ion-trap pressure, O_2 concentration and the inability to measure neutrals, or ions formed with a mass less than 50 Da. Overall, we attribute an upper limit on the uncertainty in the absolute second-order rate coefficient of 50%.

Theory

Electronic structure calculations. Gaussian 09[21] was used for all electronic structure theory calculations. Stationary points on the $C_5H_8O_5{}^{\bullet-}$ surface were characterized using the M06-2X[22] and B3LYP[23,24] density functionals using the 6-31G(2df,p) basis set. Intrinsic reaction coordinate scans were used to confirm transition state connectivity for ambiguous structures. Single point energy calculations were subsequently performed using the M06-2X geometries with the large aug-cc-pVTZ basis set. The B3LYP structures were also used in subsequent high-level energy calculations with the G3SX[25] and G4[26] methods. These two composite model chemistries calculate the total electronic energy using increasing levels of theory from HF through MP*n* to QCISD(T)/CCSD(T) for the G3SX/G4 methods, with basis sets of decreasing size. The final energy also incorporates empirical corrections based upon scaled energy increments (G3SX) or the number of paired and unpaired valence electrons (G4). The M06-2X/aug-cc-pVTZ, G3SX and G4 methods are expected to provide average errors on the order of 1–2 kcal mol^{-1},[22,25] and in particular have been selected for their excellent performance relative to cost for determining barrier heights. The coordinates of the optimized structures, vibrational frequencies and moments of inertia at the M06-2X/6-31G(2df,p) level are supplied as ESI.†

Kinetics calculations. The MultiWell2013 suite of programs[27–29] was used for statistical reaction rate simulations. Calculations were based on moments of inertia and vibrational frequencies at the M06-2X/6-31G(2df,p) level of theory, with energies from M06-2X/aug-cc-pVTZ, G3SX and G4 model chemistries.

Wells and transition states are modeled following standard statistical mechanical formulae, with internal degrees of freedom described as harmonic oscillators and external rotations treated as a separable active 1D K-rotor and inactive 2D J-rotor. Densities and sums of states were solved for energies up to 2000 cm^{-1} with a grain size of 10 cm^{-1}. The continuum master equation was then extended up to 200 000 cm^{-1}.

Collisional energy transfer between the bath gas helium and the $C_5H_8O_5^{\bullet-}$ reaction intermediate is approximated using the single-exponential down model, with a constant value of ΔE_{down}, the average energy transferred in deactivating collisions. We found that in order to achieve agreement with experiment (in which no collisionally stabilized $C_5H_8O_5^{\bullet-}$ adduct ion was detected), a ΔE_{down} of around 10 cm^{-1} was required. Note that recent modeling of energy transfer in collisions of similarly sized *cations* with helium has required ΔE_{down} values on the order of 100–300 cm^{-1},[13,30] which is considerably larger than that seen in the present *anionic* system. The latter is more consistent with accurate ΔE_{down} values recently reported for the methane–helium system at room temperature.[31]

The Lennard-Jones model is used to approximate the frequency of bath gas collisions, with σ and $\varepsilon/k_{\mathrm{b}}$ for all wells estimated as 6.3 Å and 800 K, respectively, using additivity procedures based on partial molar volumes.[32] Microcanonical rate coefficients $k(E)$ are determined from sums and densities of states along with calculated barrier heights using RRKM theory.

For barrierless association of the $^{\bullet}CH_2C(OH)(CH_3)CH_2C(O)O^-$ radical anion with O_2, the restricted Gorin model has been used to generate a representative transition state structure. Here, the high-pressure limit rate coefficient was set at the parameterized trajectory theory collision rate of 5.9×10^{-10} cm^3 $\mathrm{molecule}^{-1}$ s^{-1} at 307 K. A Morse function is used to model the dissociation potential by fitting the adiabatic 2D J-rotor of the transition state. The method employed by Golden[33] is then used to estimate the centre of mass distance at equilibrium from the reduced mass and 1D K-rotor of the complex. The restricted Gorin transition state is subsequently constructed from the 1D and 2D external rotors and the four extra degrees of freedom representing the internal rotations, along with the vibrational frequencies of the dissociated fragments.

Stochastic master equation simulations were conducted under conditions representative of the ion-trap: 307 K and 2.5 mTorr of helium. Each simulation featured 10^7 trials, which allowed us to obtain reliable statistics on channels with low yields.

Results and discussion

Mass spectrometry

The approach used to synthesize and isolate the $^{\bullet}CH_2C(OH)(CH_3)CH_2C(O)O^-$ radical anion in the gas phase is summarized in Scheme 1. The dicarboxylate dianion at *m*/*z* 80 is generated by subjecting a methanolic solution of 3-hydroxy-3-methylglutaric acid to electrospray ionization. The target radical anion is formed by mass-selecting the *m*/*z* 80 dianion population and subsequently irradiating it with a 266 nm laser pulse. Electron photodetachment and prompt decarboxylation result, yielding the product detected at *m*/*z* 116. Fig. 1 provides mass spectra demonstrating (A) isolation of the 3-hydroxy-3-methylglutaric acid dianion, (B) subsequent collision-induced dissociation (CID) and (C) photodetachment (PD) of the isolated dianion. While PD of the *m*/*z* 80 ion yields only the target ion at *m*/*z* 116 as the major product (Fig. 1C), the less-selective CID (Fig. 1B) approach predominantly leads to even-electron dissociation processes yielding product ions at *m*/*z* 59 ($C_2H_3O_2^-$) and 101 ($C_4H_5O_3^-$). In order to further investigate the nature of the *m*/*z* 116 radical anion produced according to the steps outlined in Scheme 1, it was isolated in the ion-trap and subjected to CID (see ESI,† Fig. S1). This predominantly resulted in loss of C_3H_6O to yield a product ion of *m*/*z* 58, consistent with β-scission of the target distonic radical anion. These data indicate that the product ion at *m*/*z* 116 is most likely the desired γ-carboxylate isomer and not the resonance stabilized α-carboxylate radical anion isomer, which cannot undergo a direct bond homolysis to lose C_3H_6O. We have assigned the product ion at *m*/*z* 58 as the $^{\bullet}CH_2C(O)O^-$ acetate radical anion. This assignment is supported by experiments in which the *m*/*z* 58 anion was re-isolated in the presence of O_2, where it reacted to yield a product at *m*/*z* 60, consistent with the known reaction of the acetate radical anion to form $CO_3^{\bullet-}$.[17]

Isolation of the $^{\bullet}CH_2C(OH)(CH_3)CH_2C(O)O^-$ radical anion (*m*/*z* 116) in the presence of O_2 for 10 s resulted in the mass spectrum depicted in Fig. 2. The dominant reaction products are ions corresponding to loss of 29 Da [$+O_2$ $-^{\bullet}CHO_3$] at *m*/*z* 87 and loss of 15 Da [$+O_2$ $-^{\bullet}CH_3O_2$] at *m*/*z* 101, along with a small peak at *m*/*z* 131 corresponding to [$+O_2$ $-^{\bullet}OH$]. Reaction is postulated to proceed *via* the $^{\bullet}O_2CH_2C(OH)(CH_3)CH_2C(O)O^-$ peroxyl radical intermediate depicted in Scheme 2, although there was no evidence of a product ion with mass of the stabilized peroxyl radical [$+O_2$] at *m*/*z* 148. The assignment of

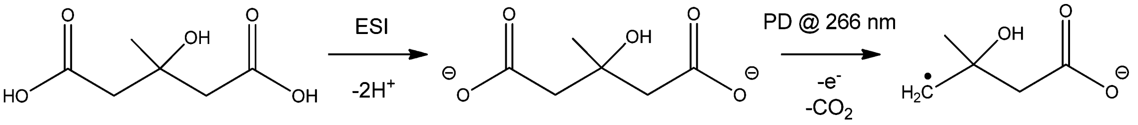

Scheme 1 Gas-phase synthesis of the β-hydroxyalkyl radical anion $^{\bullet}CH_2C(OH)(CH_3)CH_2C(O)O^-$ *via* electrospray ionization (ESI) of 3-hydroxy-3-methylglutaric acid to yield the dianion with subsequent photodissociation (PD) to produce the target radical anion at *m*/*z* 116.

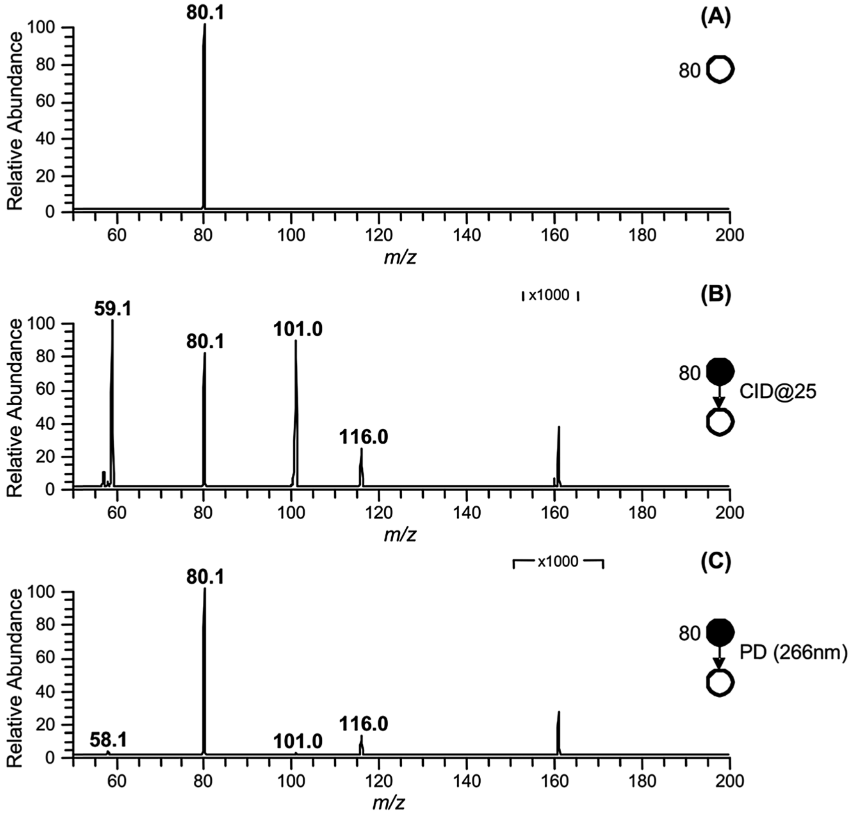

Fig. 1 (A) Isolation of the 3-hydroxy-3-methylglutaric acid dianion (*m*/*z* 80) in the gas-phase. (B) Collision induced dissociation (CID) of *m*/*z* 80. (C) Photodissociation (PD) of *m*/*z* 80.

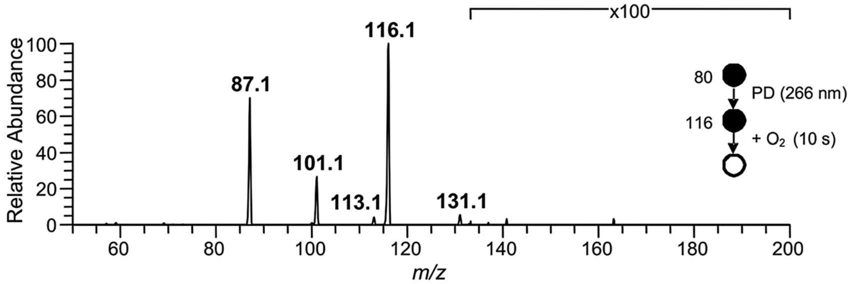

Fig. 2 Mass spectrum resulting from the $^\bullet CH_2C(OH)(CH_3)CH_2C(O)O^-$ (*m*/*z* 116) radical anion reaction with O_2 after 10 s of reaction time. The *m*/*z* 116 ion was synthesized in the gas-phase following Scheme 1, and was isolated in the presence of 3.1×10^9 molecule cm^{-3} O_2.

the radical anion to the γ-carboxylate isomer, rather than the α-carboxylate isomer, is further supported by the absence of a carbonate radical anion signal at *m*/*z* 60 in the O_2 reaction experiments. Decay of the parent ion with respect to time was followed over the course of 10 s, with the kinetics found to exhibit good pseudo first-order behavior (ESI†). These observations further support the assertion that the *m*/*z* 116 ion population consists of a single reactive isomer assigned here to the γ-carboxylate radical ion shown in Scheme 2. Finally, given the known O_2 concentration of $(3.1 \pm 0.1) \times 10^9$ molecule cm^{-3} and measured first-order rate coefficient of 0.071 ± 0.001 s^{-1}, the second-order rate coefficient for the $^\bullet CH_2C(OH)(CH_3)CH_2C(O)O^-$ + O_2 reaction can be deduced as $(2.3 \pm 0.1) \times 10^{-11}$ cm^3 molecule^{-1} s^{-1}. Considering the ion–molecule collision rate of 5.9×10^{-11} cm^3 molecule^{-1} s^{-1}, the reaction efficiency is determined to be 3.9%.

We hypothesize that the products detected in the $^\bullet CH_2C(OH)(CH_3)CH_2C(O)O^- + O_2$ reaction arise from chemically activated fragmentation of the $^\bullet O_2CH_2C(OH)(CH_3)CH_2C(O)O^-$ peroxyl radical intermediate within the low pressure conditions of the ion-trap. *Vide infra*, the product ion at *m*/*z* 87 is suggested to arise from concerted loss of $^\bullet$OH and formaldehyde (*i.e.*, +O_2 –$^\bullet$OH –HCHO), whereas the product ion at *m*/*z* 101 is attributed to a two-stage reaction in which the $^\bullet$OH radical is first eliminated, followed by rapid decarboxylation from the vibrationally hot *m*/*z* 131 product ion population (*i.e.*, + O_2 –$^\bullet$OH –CO_2). The product detected at *m*/*z* 131 is suggestive of minor collisional deactivation of these [+O_2 –$^\bullet$OH] ions prior

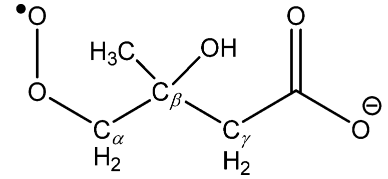

Scheme 2 Structure and nomenclature for the β-hydroxyperoxyl radical $^{\bullet}O_2CH_2C(OH)(CH_3)CH_2C(O)O^-$ (**W1**). The C_γ abstraction channel proceeds through a 1,5-hydrogen shift from the γ-methylene group and the OH abstraction channel proceeds through 1,5-hydrogen shift from the β-hydroxyl group (relative to the peroxyl functionality).

to decarboxylation, or the formation of a stable [$+O_2$ $-^{\bullet}OH$] isomer in small yield.

To gain insight into the reaction mechanism and assist with product assignments, experiments utilizing $^{18}O_2$ and the deuterated isotopologue $^{\bullet}CH_2C(OD)(CH_3)CH_2C(O)O^-$ were carried out, and the resulting mass spectra are provided in the ESI.† When $^{\bullet}CH_2C(OH)(CH_3)CH_2C(O)O^-$ was isolated in the presence of $^{18}O_2$, the major product ion previously identified at *m*/*z* 87 shifts to 89, whereas the product observed at *m*/*z* 101 remains unchanged. This indicates that the *m*/*z* 87 product is incorporating one of the oxygen atoms from $^{18}O_2$, whereas the *m*/*z* 101 product does not contain any oxygen from $^{18}O_2$. Note also that the minor peak observed at *m*/*z* 131 shifts to 133, consistent with loss of $^{\bullet 18}OH$ from a peroxyl radical intermediate. Exchange of the hydroxyl group to deuterated hydroxyl (OD) was achieved by electrospray of the precursor in D_1-methanol. Reaction of $^{\bullet}CH_2C(OD)(CH_3)CH_2C(O)O^-$ with O_2 reveals that the product ions previously observed at *m*/*z* 87 and 101 actually each comprise two separable isomers, with peaks now appearing at *m*/*z* 87, 88, 101 and 102. Relative intensities for the *m*/*z* 87 and 88 peaks and for the *m*/*z* 101 and 102 peaks are of similar magnitude. This indicates that reactions are proceeding at similar rates *via* reaction at the OD group and *via* some other mechanism involving C–H bond activation. The minor product channel previously observed at *m*/*z* 131 remains largely unchanged, indicating that it predominantly corresponds to $^{\bullet}OD$ loss from the peroxyl radical intermediate.

Reaction mechanism

A potential energy surface for the $^{\bullet}CH_2C(OH)(CH_3)CH_2C(O)O^-$ + O_2 reaction system is provided in Fig. 3. Secondary decarboxylation reactions for the initial reaction products leading to CO_2 loss, as will be discussed below, are demonstrated in Fig. 4. Optimized structures of the wells and transition states at the M06-2X/aug-cc-pVTZ level of theory are illustrated in Fig. 5 and 6 respectively. As can be seen in Fig. 3 and 4, the three theoretical methods are in relatively good agreement, with the G4 to G3SX and G4 to M06-2X average deviations being 2.2 kcal mol^{-1} and 1.6 kcal mol^{-1} respectively. These are consistent with the expected mean errors of 1–2 kcal mol^{-1}.[22,25,26]

Fig. 3 shows that the initial reaction begins with barrierless addition of O_2 to the radical, resulting in formation of the β-hydroxyperoxyl radical $^{\bullet}O_2CH_2C(OH)(CH_3)CH_2C(O)O^-$ (**W1**). This reaction is exothermic by 39 kcal mol^{-1}, providing the chemically activated peroxyl radical intermediate with considerable excess vibrational energy. **W1** may then proceed with a series of unimolecular transformations, encountering barriers at around or below the entrance channel energy. Specifically, two branches were identified for the subsequent reactions of **W1** (see Scheme 2 for nomenclature) that lead to expulsion of $^{\bullet}OH$ through 1,5-hydrogen shifts from the γ-methylene group (C_γ abstraction) and from the β-hydroxyl group (OH abstraction).

1,5-Hydrogen abstraction from the γ-methylene group proceeds *via* **TS1**, with a barrier around 14 kcal mol^{-1} below the initial reactants (or 25 kcal mol^{-1} above the **W1** energy). This reaction produces a hydroperoxide-substituted radical anion (**W2**) which can decompose to three distinct product sets, labeled **P1** + $^{\bullet}OH$, **P2** + $^{\bullet}OH$ + HCHO and **P3** + $^{\bullet}OH$. First, homolytic substitution *via* the hydroperoxide group results in the four-member ring structure **P1** + $^{\bullet}OH$. This reaction has a barrier predicted to be around that of the reactants (only 0.4 kcal mol^{-1} below the reactants at the G4 level) and is thus unlikely to be of major significance. Second, HCHO and $^{\bullet}OH$ can be eliminated from **W2** by β-scission (**TS3**), leading to an enol (**P2**) + $^{\bullet}OH$ + HCHO. The barrier height here is calculated to be about 6 kcal mol^{-1} below the reactants. Third, an $^{\bullet}OH$ elimination reaction – which is effectively a proton transfer

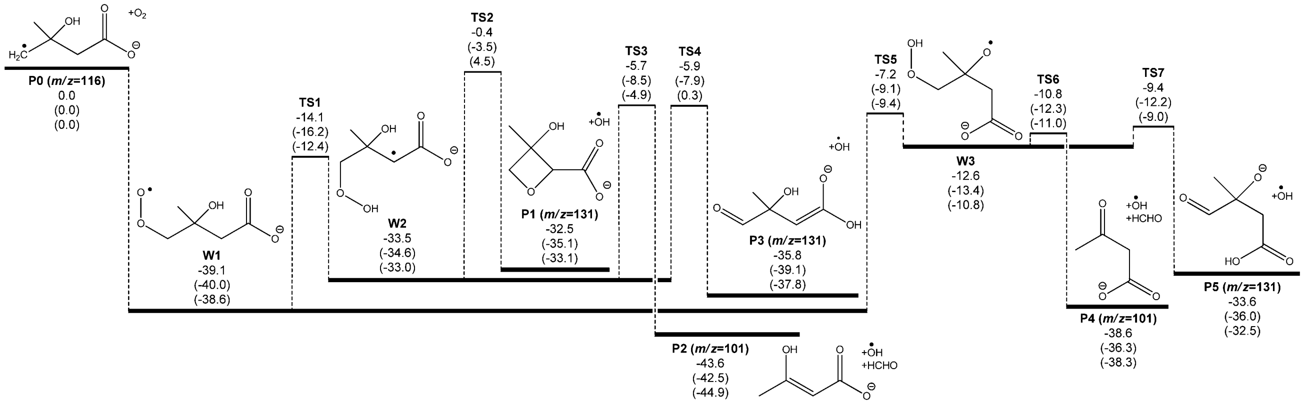

Fig. 3 *Ab initio* potential energy surface of the radical anion $^{\bullet}CH_2C(OH)(CH_3)CH_2C(O)O^-$ + O_2 reaction. Energies at 0 K with zero point energy (E_0 + ZPE) are shown at the G4/G3SX/M06-2X/aug-cc-pVTZ levels of theory, in units of kcal mol^{-1}. The mass to charge ratio (*m*/*z*) are indicated for product ions.

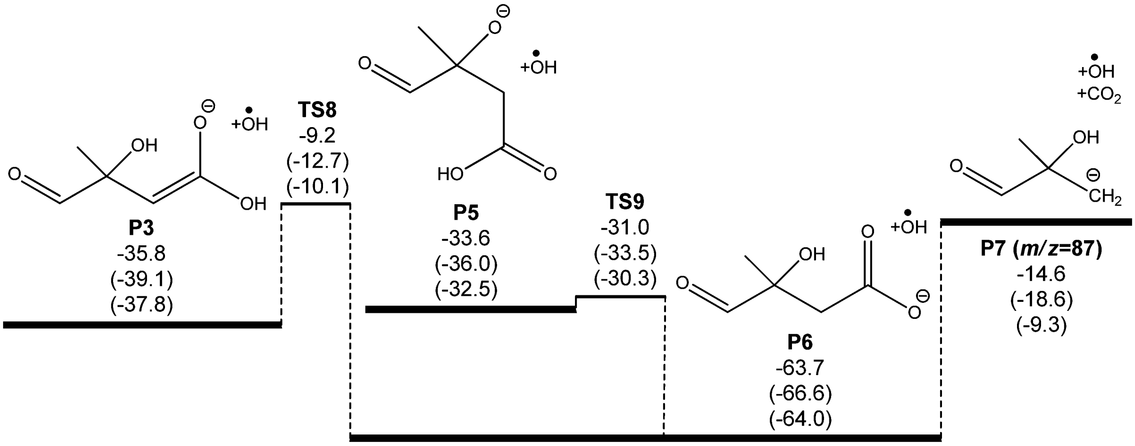

Fig. 4 *Ab initio* potential energy surface for subsequent decarboxylation of the $C_5O_4H_7^-$ anions formed *via* •OH loss in the $^{\bullet}CH_2C(OH)(CH_3)CH_2C(O)O^-$ + O_2 reaction. Energies at 0 K with zero point energy (E_0 + ZPE) are shown at the G4/G3SX/M06-2X/aug-cc-pVTZ levels of theory, in units of kcal mol^{-1}. Note that **P7** is expected to rearrange to the more stable alkoxide form $CH(O)C(CH_3)_2O^-$ when detected at *m*/*z* 87.

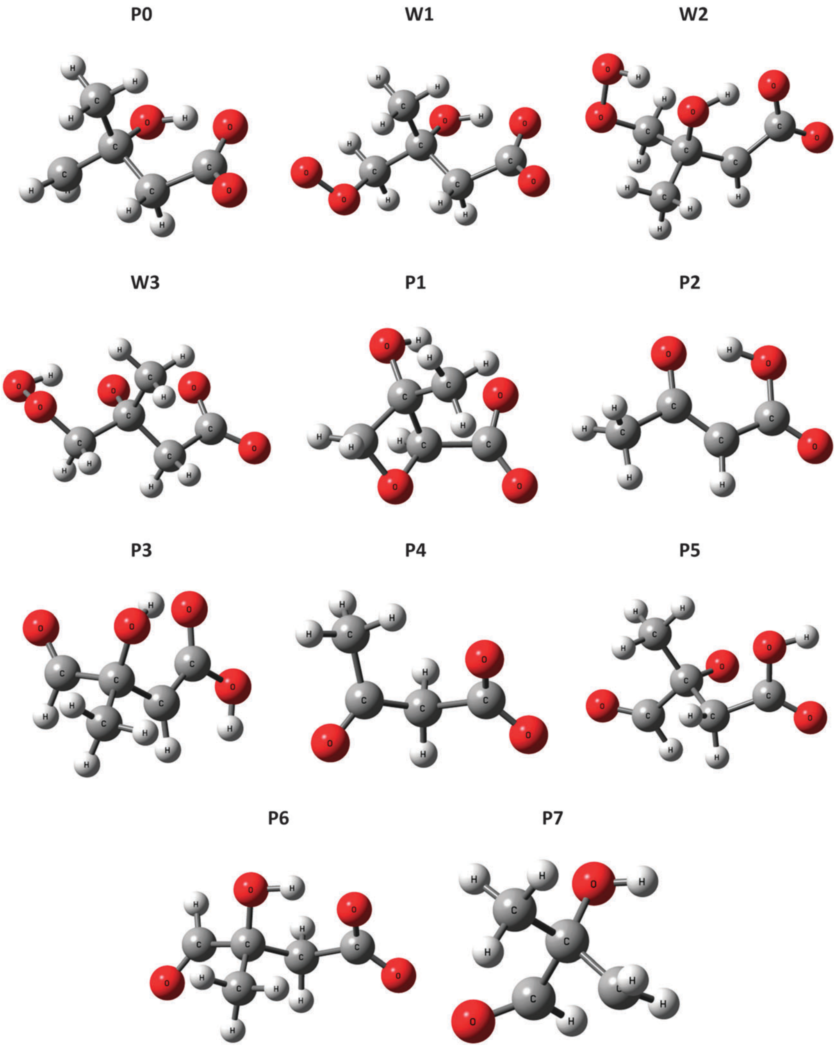

Fig. 5 Optimized structures for wells (W*n*) and product ions (P*n*) in the $^{\bullet}CH_2C(OH)(CH_3)CH_2C(O)O^-$ + O_2 reaction system, at the M06-2X level of theory.

from the alkyl peroxide moiety to the carboxylate group coupled with electron transfer – can also transpire (**TS4**), leading to an enolate anion (**P3**) + •OH. This process has analogy to the hydroxide elimination of alkyl hydroperoxides, which is driven

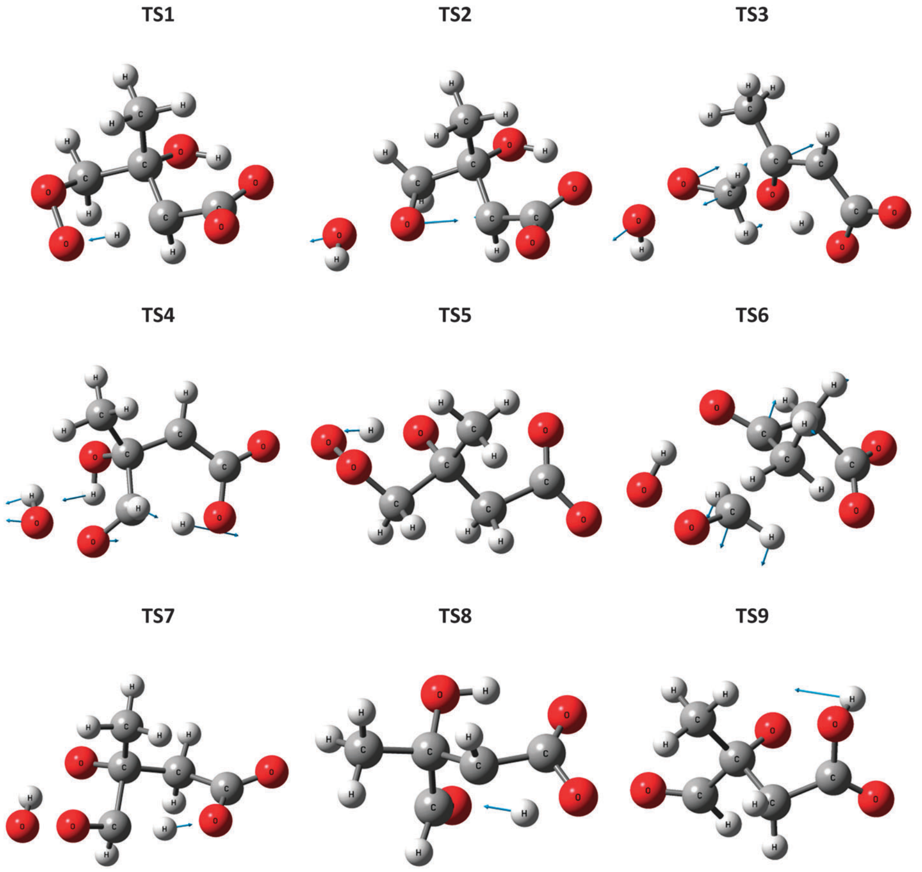

Fig. 6 Optimized structures for transition states (TS*n*) in the $^{\bullet}CH_2C(OH)(CH_3)CH_2C(O)O^-$ + O_2 reaction system, at the M06-2X level of theory. Displacement vectors for imaginary frequencies are shown.

by the weak O–O bond in the hydroperoxide group.[34] The barrier associated with **TS4** is very similar to that for **TS3**, except at the M06-2X level of theory, where it is 0.3 kcal mol^{-1} above the reactants. From the C_γ abstraction channel, product sets **P2** + $^{\bullet}$OH + HCHO and **P3** + $^{\bullet}$OH would be expected to dominate, with the relative energies of **TS3** and **TS4** controlling the reaction flux and subsequent branching ratios for these channels.

The significantly higher relative energy for **TS4** at the M06-2X level of theory, in comparison to the composite G4 and G3SX energies is intriguing and worthy of closer examination. Our kinetic modeling (*vide infra*) points to a **TS4** energy that should be below that of **TS3**, whereas the M06-2X calculations place it 5 kcal mol^{-1} higher. The G4 and G3SX calculations, on the other hand, result in energies for **TS3** and **TS4** that are almost identical. Examining the composite energy calculations, the CCSD(T) and MP4(SDTQ) energy components demonstrate an unusually large contribution from triple excitations. This component of the correlation energy dominates the other terms and is on average about 6 kcal mol^{-1} greater (more stabilizing) than the same triples energies in the reactant (**W2**) energy calculations. We suggest that the DFT calculation fails to capture a substantial component of this correlation energy resulting in a significant overestimation of the barrier height. Indeed the composite energy calculations may themselves be underestimating this correlation energy, given that the experiments suggest that **TS4** is more stable than **TS3**.

The 1,5-hydrogen shift from the β-hydroxyl group yields a hydroperoxyalkoxyl radical anion (**W3**) through **TS5**. The barrier height is calculated to be 7 kcal mol^{-1} below the reactants using G4 energies, and it is about 32 kcal mol^{-1} above the peroxyl radical. This places it very close in energy to the controlling transition states (**TS3** and **TS4** in particular) in the competing C_γ abstraction channel. The hydroperoxyalkoxyl intermediate (**W3**) lies just below the energy of **TS5**, and it can also undergo a variety of fragmentations. Simple β-scission in **W3** *via* **TS6** leads to product ion **P4** *via* concerted loss of HCHO and $^{\bullet}$OH. The barrier height for **TS6** is only 2 kcal mol^{-1} above **W3**. Alternatively, another proton transfer from the γ-methylene to the carboxylate group is available *via* **TS7**, releasing $^{\bullet}$OH and yielding an oxyanion compound (**P5**) and $^{\bullet}$OH. The barrier of this reaction is also small; it is about 1 kcal mol^{-1} greater than the energy of **TS6** but still below the energy for the initial 1,5-hydrogen shift. For the OH abstraction channel, we observe that **TS5** is likely to dominate the transmission of overall reaction flux, whereas **TS6** and **TS7** will ultimately control the branching to products. One should also notice that other potential β-fragmentation may occur. The hydroperoxyalkoxyl radical anion (**W3**) can also decompose to lose $^{\bullet}CH_3$ and $^{\bullet}CH_2C(O)O^-$. However, calculations show that the corresponding transition states for these processes are above the reactant energies and therefore not competitive. This is consistent with the experimental results observed, where there is an absence of peaks at *m*/*z* 133 and 58 respectively.

Considering the entire mechanism developed for the $^{\bullet}CH_2C(OH)(CH_3)CH_2C(O)O^- + O_2$ reaction, the four expected dominant product sets originate *via* transition states that are all very close in energy, grouped at 5 to 10 kcal mol^{-1} below the reactant energies. This mechanism can explain the experimental observation of an *m*/*z* 101 product anion [$+O_2$ $-^{\bullet}OH$ $-HCHO$] in the mass spectrometry experiments. However it also seems to suggest substantial formation of an *m*/*z* 131 anion [$+O_2$ $-^{\bullet}OH$], as opposed to the major *m*/*z* 87 product anion that is detected. This apparent discrepancy can be resolved by considering further CO_2 elimination from the dominant closed-shell anions that arise from $^{\bullet}OH$ loss in the $^{\bullet}CH_2C(OH)(CH_3)CH_2C(O)O^- + O_2$ reaction (**P3** and **P5**). An energy diagram for this process is depicted in Fig. 4, where all energies are relative to the initial reactants ($^{\bullet}CH_2C(OH)(CH_3)CH_2C(O)O^- + O_2$). Note that the $^{\bullet}OH$ radical is included in the energy calculations (and therefore energy diagram) only so that energies are relative to the initial reactants. The $^{\bullet}OH$ radical here is an infinitely separated product.

The oxyanion structure (**P5**) can readily undergo internal proton transfer (**TS9**) to yield a significantly more stable carboxylate anion (**P6**). The transition state structure here is peculiar, as the imaginary frequency corresponds to internal rotation about the carboxyl C–OH bond. Referring to Fig. 7, intrinsic reaction coordinate scans reveal that following internal rotation the proton spontaneously migrates to the O^- site, exothermically generating the carboxylate anion structure (**P6**). From here, barrierless C–C bond scission releases CO_2, leaving a carbanion (**P7**). This final step proceeds with the highest energy, but is about 15 kcal mol^{-1} below the initial $^{\bullet}CH_2C(OH)(CH_3)CH_2C(O)O^- + O_2$ energy. Assuming prompt internal energy redistribution, and that little energy is lost *via* collisional deactivation or to translational energy upon $^{\bullet}OH$ ejection, it is plausible that a significant portion of the vibrationally-hot product ion population arising from **TS7** will have sufficient energy to undergo this further decarboxylation mechanism, consistent with the experimental observations. It is anticipated, however, that following dissociation the depicted carbanion (**P7**) would rearrange to the more stable alkoxide form $CH(O)C(CH_3)_2O^-$ to yield the actual product anion observed at *m*/*z* 87.

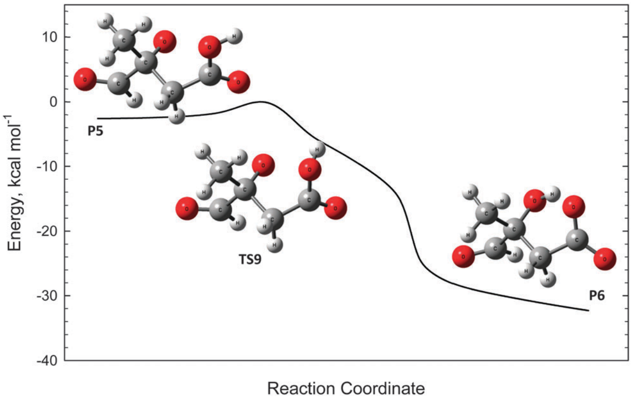

Fig. 7 Intrinsic reaction coordinate scan for the ambiguous transition state structure **TS9**. The scan confirms the connectivity of **TS9** to the reactant **P5** and product **P6**.

For the enolate anion (**P3**) produced *via* $^{\bullet}OH$ loss through **TS4** in the primary $^{\bullet}CH_2C(OH)(CH_3)CH_2C(O)O^- + O_2$ mechanism, a similar decarboxylation process is available. Here, the proton transfer *via* **TS8** required to yield the intermediate **P6** has a considerable barrier, at 10 kcal mol^{-1} below the starting reactants, and is likely to be the rate controlling step for decarboxylation. However, this mechanism does again provide an explanation for the observation of an *m*/*z* 87 product ion (and not *m*/*z* 131) in the $^{\bullet}CH_2C(OH)(CH_3)CH_2C(O)O^- + O_2$ reaction.

The potential energy diagram can explain all major products observed experimentally from the $^{\bullet}CH_2C(OH)(CH_3)CH_2C(O)O^- + O_2$ reaction. Based on the mass spectrometry analysis, the three major products from the reaction of the radical anion $^{\bullet}CH_2C(OH)(CH_3)CH_2C(O)O^- + O_2$ have *m*/*z* of 131, 101, and 87, which corresponds to [$+O_2$ $-^{\bullet}OH$], [$+O_2$ $-^{\bullet}OH$ $-HCHO$], and [$+O_2$ $-^{\bullet}OH$ $-CO_2$] respectively. The proposed mechanism is also consistent with the $^{18}O_2$ experiments, with the product sets corresponding to *m*/*z* 101 (**P2** + $^{\bullet}OH$ + HCHO and **P4** + $^{\bullet}OH$ + HCHO) formed through loss of both of the added oxygen atoms, whereas the product corresponding to *m*/*z* 87 ($CH(O)C(CH_3)_2O^-$ + $^{\bullet}OH$ + CO_2) retains one of the atoms from O_2. Because the two proposed product channels accessed *via* initial C_γ abstraction and OH abstraction channels yield isobaric ions, they cannot be differentiated in the mass spectrometry experiments using unlabelled $^{\bullet}CH_2C(OH)(CH_3)CH_2C(O)O^-$, although they can be identified in the deuterated isotopologue case ($^{\bullet}CH_2C(OD)(CH_3)$-$CH_2C(O)O^-$). For the latter, initial reaction *via* OD abstraction would always result in $^{\bullet}OD$ loss, whereas initial abstraction from the C_γ group would yield $^{\bullet}OH$ (see ESI† for reaction schemes). Our experiments therefore provide evidence for $^{\bullet}OH$ (then CO_2) and $^{\bullet}OH$ + HCHO loss in the chemically activated peroxyl radical proceeding *via* both 1,5-hydrogen atom transfer mechanisms.

It is of interest to relate the calculations reported here to the analogous neutral peroxyl radical $^{\bullet}O_2CH_2C(OH)(CH_3)CH_2C(O)OH$, in which the carboxylate group has been protonated. Calculations show that the relevant product channels are still accessible, with transition states being below the entrance channel. The G4 reaction barriers of **TS1** and **TS5** (see Fig. 3) are 25.0 kcal mol^{-1} and 31.9 kcal mol^{-1} for the radical anion respectively. These barriers are calculated to be 28.2 kcal mol^{-1} and 27.7 kcal mol^{-1} for the neutral radical form.

Reaction kinetics

Master equation simulations were performed to further investigate the $^{\bullet}CH_2C(OH)(CH_3)CH_2C(O)O^- + O_2$ reaction system and validate the theoretically proposed reaction mechanism. The M06-2X structures were used in all simulations, along with barrier heights evaluated at the three tested levels of theory (M06-2X, G3SX and G4). The simulated time evolution of the wells and products using G4 energies is illustrated in Fig. 8, with the corresponding figures using M06-2X and G3SX energies

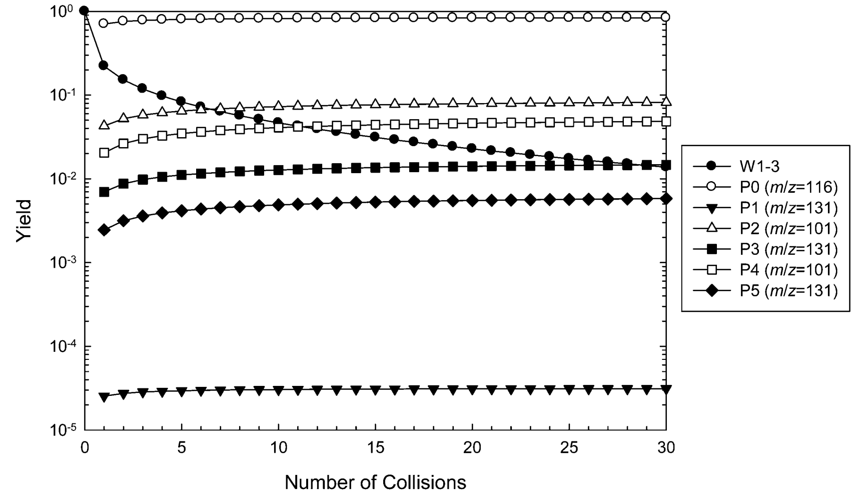

Fig. 8 Master equation simulation for the $^\bullet CH_2C(OH)(CH_3)CH_2C(O)O^-$ + O_2 reaction at 307 K and 2.5 mTorr of helium, using G4 barrier heights. Results are presented as yields of wells and product ions as a function of the number of collisions. Note that the *m*/*z* 131 product ions **P3** and **P5** are also responsible for the peaks detected at *m*/*z* = 87 following decarboxylation.

provided in ESI.† The results of these calculations are tabulated in Table 1, where they are also compared with the experimental data. The master equation modeling applies to the dissociation of initially activated $^\bullet O_2CH_2C(OH)(CH_3)CH_2C(O)O^-$ (**W1**), which can be collisionally deactivated as any of the interconnected wells (**W1, W2, W3**), undergo reverse reaction to $^\bullet CH_2C(OH)(CH_3)CH_2C(O)O^-$ + O_2, or dissociate to the five product sets corresponding to the [+O_2 −$^\bullet$OH −HCHO] (*m*/*z* 101) and [+O_2 −$^\bullet$OH] (*m*/*z* 131) channels. Note that the subsequent decarboxylation reactions of the hot *m*/*z* 131 anions are not included in the master equation modeling, and we make the assumption that this process occurs quantitatively.

Referring to Fig. 8, the relative concentration (yield) of all intermediate wells and product sets involved in the reaction are plotted as a function of number of collisions (the sum of yields is 100% at any given time). The majority (80%) of the excited adduct population dissociates back to the reactants, resulting in a predicted reaction efficiency of about 20%. This result is relatively insensitive to the level of theory. Using G4 energies, about two-thirds of the remaining peroxyl radical population is predicted to react *via* the C_γ abstraction channel to produce **P2** + $^\bullet$OH + HCHO (54%, *m*/*z* 101) and **P3** + $^\bullet$OH (10%, *m*/*z* 131), with the rest proceeding through the OH abstraction channel to yield **P4** + $^\bullet$OH + HCHO (33%, *m*/*z* 101) and **P5** + $^\bullet$OH (4%, *m*/*z* 131). Again, similar results are obtained at the other levels of theory. The prediction of relatively similar branching ratios between the alternative C_γ and OH abstraction channels is consistent with the isotope labeling studies. Referring to Table 1, all simulations favor the [+O_2 −$^\bullet$OH −HCHO] (*m*/*z* 101) product channels over [+O_2 −$^\bullet$OH −CO_2] (*m*/*z* 87) following both hydrogen abstraction pathways, whereas the experiments find the opposite. This can be attributed to the similarity in the energies of **TS3** and **TS4**, and **TS6** and **TS7**, where differences are within the expected accuracy of the theoretical methods. Decarboxylation would be expected to dominate if the barriers associated with **TS4** and **TS7** were above those of **TS3** and **TS6**, respectively. However, G4 energy calculations find that **TS3** is 0.2 kcal mol^{-1} above **TS4**, whereas **TS7** is 1.4 kcal mol^{-1} above **TS6**. Note also that in order for these results to be compatible with the experimental observations, we must assume that the vibrationally excited *m*/*z* 131 anions corresponding to product sets **P3** + $^\bullet$OH and **P5** + $^\bullet$OH undergo further decarboxylation to the *m*/*z* 87 product + $^\bullet$OH + CO_2 almost completely. The experimental detection of some small yield of an *m*/*z* 131 product ion could perhaps be explained by **P1** + $^\bullet$OH, which has a relatively large barrier height, or more likely by minor collisional deactivation of the *m*/*z* 131 ions arising from **P3** + $^\bullet$OH and **P5** + $^\bullet$OH.

Table 1 Rate coefficients (*k*), reaction efficiencies (*ϕ*), and product branching fractions for the $^\bullet CH_2C(OH)(CH_3)CH_2C(O)O^-$ + O_2 reaction, from experiment and theory. Theoretical kinetic simulations were performed using energies at three different levels of theory (G4, G3SX, M06-2X), and with inclusion of a pre-reaction complex ("pre"). Note that the $^\bullet$OH loss channels will subsequently lose CO_2 through decarboxylation

	k (cm^3 molecule^{-1} s^{-1})	*ϕ* (%)	$^\bullet$OH loss (%)	$^\bullet$OH, HCHO loss (%)
Experiment	2.3×10^{-11}	3.9	73	27
Theory (G4)	9.5×10^{-11}	16.2	14	85
Theory (G4 + pre)	7.6×10^{-13}	0.1	13	87
Theory (G3SX)	3.4×10^{-10}	57.8	8	91
Theory (M06-2X)	2.1×10^{-10}	34.8	7	90

The predicted reaction efficiency and, therefore, the rate coefficient obtained from the master equation simulations is much higher than that found experimentally. The low reaction efficiency identified for this reaction is similar to values obtained for other distonic radical reactions with O_2.[35] However, it is discordant with the high efficiencies measured for related α-carboxylate radical anion reactions with O_2.[13] Indeed, in the glycyl radical anion + O_2 reaction the reaction efficiency was measured as being effectively 100%, and this number could be accurately reproduced by master equation simulations similar to

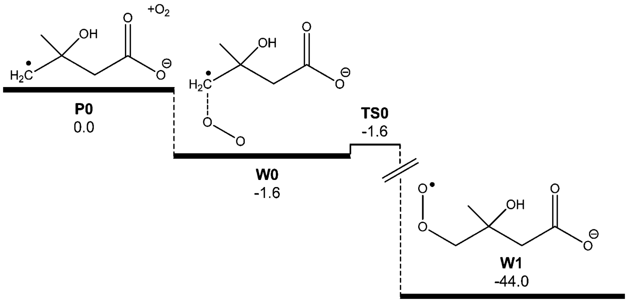

Fig. 9 *Ab initio* potential energy surface of the proposed pre-reaction complex **W0**. Energies at 0 K (E_0) are provided at the M06-2X/6-31+G(2df,p) level of theory in kcal mol^{-1}.

those carried out here.[13] The low reaction efficiency measured in the present work indicates some additional restriction to peroxyl radical formation, resulting in significant reflection of the nascent $[C_5O_5H_8^{\bullet -}]^*$ adduct population back to $^{\bullet}CH_2C(OH)(CH_3)CH_2C(O)O^- + O_2$ before the peroxyl radical can form and subsequently dissociate to new products. To incorporate this phenomenon into our reaction rate model we investigated the possibility of a pre-reaction complex occurring along the $O_2\cdots{}^{\bullet}CH_2C(OH)(CH_3)CH_2C(O)O^-$ reaction coordinate. Although a pre-reaction complex was not identified at the M06-2X/6-31G(2df,p) level of theory, one could be located when diffuse basis functions were added to the basis set (*i.e.*, 6-31+G(2df,p)). Referring to Fig. 9, this pre-reaction complex sits at 0.7 kcal mol^{-1} below the reactant energy. A transition state structure was also identified just 0.06 kcal mol^{-1} above the complex energy, or 0.15 kcal mol^{-1} below it when zero point energies are included. It is of relevance to note that the inclusion of diffuse functions has a negligible effect on both structure and energy of the reactants $^{\bullet}CH_2C(OH)(CH_3)CH_2C(O)O^- + O_2$ or the peroxyl radical $CH_2C(OH)(CH_3)CH_2C(O)O^-$ themselves.

This new two-transition-state model of $^{\bullet}O_2CH_2C(OH)(CH_3)CH_2C(O)O^-$ formation was incorporated into the master equation model. The results of the new simulations are depicted in Fig. 10 using G4 energies, and are also included in Table 1. We now observe major reflection of the chemically activated peroxyl radical population back to the reactants, with only around 0.1% of the adduct going on to form new products. All other product channels are predicted to form in the same preferential order as shown in Fig. 9. This presence of the pre-reaction complex dramatically reduces the calculated rate coefficient, with the predictions now being slower than expected. This would appear to support the presence of a lower lying pre-reaction complex than that identified here, or merely an inflection on the bond dissociation potential, and more in-depth variational transition state theory modeling may be necessary to better describe this behavior.

Conclusion

A distonic β-hydroxylalkyl radical analogue $^{\bullet}CH_2C(OH)(CH_3)CH_2C(O)O^-$ has been generated by ion-trap mass spectrometry. Reaction of the β-hydroxylalkyl radical in the presence of O_2 proceeded with a second order rate of 2.3×10^{-11} cm^3 molecule^{-1} s^{-1} corresponding to a reaction efficiency of 3.9%. Products were identified consistent with initial formation of a β-hydroxyalkylperoxyl radical that may undergo facile unimolecular decomposition reactions *via* 1,5-hydrogen atom abstractions from the γ-methylene and β-hydroxyl positions to yield ions at *m*/*z* 131, 101 and 87 due to neutral loss of $^{\bullet}OH$, $^{\bullet}OH$ + HCHO, and $^{\bullet}OH + CO_2$, respectively. A theoretical study of the reaction mechanism revealed pathways to all major experimental products, and master equation simulations were performed to gain further insight into the reaction kinetics and product branching. In several of the mechanisms identified, the charge tag ($-CO_2^-$) does not participate directly in the transformation (pathways to **P1**, **P2** and **P4** formation in Fig. 3) suggesting that these pathways may have analogy for the neutral system. While we are cognizant that even remote

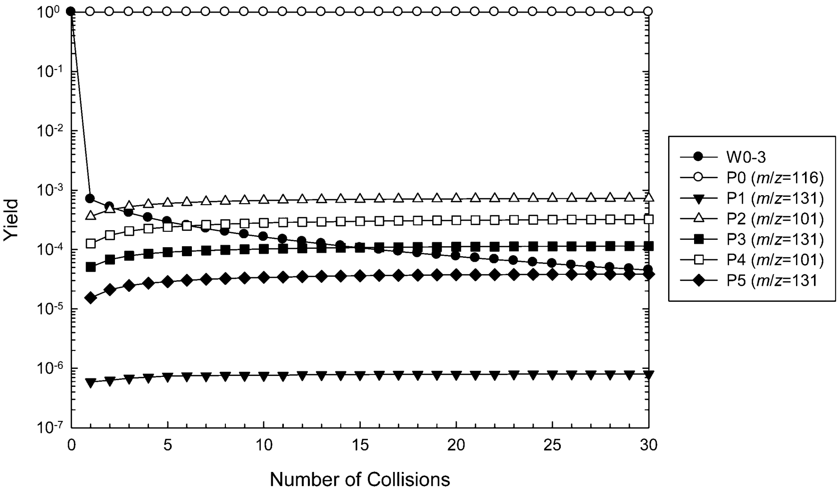

Fig. 10 Master equation simulation for the $^{\bullet}CH_2C(OH)(CH_3)CH_2C(O)O^- + O_2$ reaction at 307 K and 2.5 mTorr of helium, including the pre-reaction complex **W0**, using G4 barrier heights. Results are presented as yields of wells and product ions as a function of number of collisions. Note that the *m*/*z* 131 product ions **P3** and **P5** are also responsible for the peaks detected at *m*/*z* = 87 following decarboxylation.

anions can influence radical stability and thus energetics,[36,37] the proposed reaction mechanism of the $^{\bullet}CH_2C(OH)(CH_3)CH_2C(O)O^- + O_2$ reaction still serves as a model to reveal the unimolecular decomposition chemistry of peroxyl radicals formed in biogenic VOC oxidation that can replenish $^{\bullet}OH$ in the troposphere.

Acknowledgements

The authors are grateful to the Australian Research Council for funding through the Discovery Project (DP110103889 [GdS], DP140101237 [SJB], DP130100862 [AJT & GdS]), Centre of Excellence Grant (CE0561607 [SJB]) and Future Fellowship (FT130101304 [GdS]) schemes.

References

1 D. Pierotti, S. Wofsy, D. Jacob and R. Rasmussen, *J. Geophys. Res.*, 1990, **95**, 1871–1881.
2 S. Montzka, M. Trainer, P. Goldan, W. Kuster and F. Fehsenfeld, *J. Geophys. Res.*, 1993, **98**, 1101–1111.
3 C. Warneke, R. Holzinger, A. Hansel, A. Jordan, W. Lindinger, U. Pöschl, J. Williams, P. Hoor, H. Fischer and P. Crutzen, *J. Atmos. Chem.*, 2001, **38**, 167–185.
4 M. Claeys, B. Graham, G. Vas, W. Wang, R. Vermeylen, V. Pashynska, J. Cafmeyer, P. Guyon, M. O. Andreae and P. Artaxo, *Science*, 2004, **303**, 1173–1176.
5 J. H. Kroll, N. L. Ng, S. M. Murphy, R. C. Flagan and J. H. Seinfeld, *Environ. Sci. Technol.*, 2006, **40**, 1869–1877.
6 D. K. Henze and J. H. Seinfeld, *Geophys. Res. Lett.*, 2006, **33**, L09812.
7 N. Poisson, M. Kanakidou and P. J. Crutzen, *J. Atmos. Chem.*, 2000, **36**, 157–230.
8 D. Tan, I. Faloona, J. B. Simpas, W. Brune, P. B. Shepson, T. L. Couch, A. L. Sumner, M. A. Carroll, T. Thornberry, E. Apel, D. Riemer and W. Stockwell, *J. Geophys. Res.*, 2001, **106**, 24407–24427.
9 G. da Silva, C. Graham and Z. F. Wang, *Environ. Sci. Technol.*, 2009, **44**, 250–256.
10 J. Peeters, T. L. Nguyen and L. Vereecken, *Phys. Chem. Chem. Phys.*, 2009, **11**, 5935–5939.
11 B. B. Kirk, D. G. Harman and S. J. Blanksby, *J. Phys. Chem. A*, 2009, **114**, 1446–1456.
12 B. B. Kirk, D. G. Harman, H. I. Kenttämaa, A. J. Trevitt and S. J. Blanksby, *Phys. Chem. Chem. Phys.*, 2012, **14**, 16719–16730.
13 G. da Silva, B. B. Kirk, C. Lloyd, A. J. Trevitt and S. J. Blanksby, *J. Phys. Chem. Lett.*, 2012, **3**, 805–811.
14 M. B. Prendergast, P. A. Cooper, B. B. Kirk, G. da Silva, S. J. Blanksby and A. J. Trevitt, *Phys. Chem. Chem. Phys.*, 2013, **15**, 20577–20584.
15 C. H. Li, G. N. Khairallah, A. K. Lam, R. A. O'Hair, B. B. Kirk, S. J. Blanksby, G. da Silva and U. Wille, *Chem. – Asian J.*, 2013, **8**, 450–464.
16 G. N. Khairallah, R. A. O'Hair and U. Wille, *J. Phys. Chem. A*, 2014, **118**, 3295–3306.
17 T. Ly, B. B. Kirk, P. I. Hettiarachchi, B. L. Poad, A. J. Trevitt, G. da Silva and S. J. Blanksby, *Phys. Chem. Chem. Phys.*, 2011, **13**, 16314–16323.
18 D. G. Harman and S. J. Blanksby, *Org. Biomol. Chem.*, 2007, **5**, 3495–3503.
19 T. Ly and R. R. Julian, *Angew. Chem., Int. Ed.*, 2009, **48**, 7130–7137.
20 T. Y. Kim, M. S. Thompson and J. P. Reilly, *Rapid Commun. Mass Spectrom.*, 2005, **19**, 1657–1665.
21 M. J. Frisch, G. W. Trucks, H. B. Schlegel, G. E. Scuseria, M. A. Robb, J. R. Cheeseman, G. Scalmani, V. Barone, B. Mennucci, G. A. Petersson, H. Nakatsuji, M. Caricato, X. Li, H. P. Hratchian, A. F. Izmaylov, J. Bloino, G. Zheng, J. L. Sonnenberg, M. Hada, M. Ehara, K. Toyota, R. Fukuda, J. Hasegawa, M. Ishida, T. Nakajima, Y. Honda, O. Kitao, H. Nakai, T. Vreven, J. A. Montgomery Jr., J. E. Peralta, F. Ogliaro, M. Bearpark, J. J. Heyd, E. Brothers, K. N. Kudin, V. N. Staroverov, T. Keith, R. Kobayashi, J. Normand, K. Raghavachari, A. Rendell, J. C. Burant, S. S. Iyengar, J. Tomasi, M. Cossi, N. Rega, J. M. Millam, M. Klene, J. E. Knox, J. B. Cross, V. Bakken, C. Adamo, J. Jaramillo, R. Gomperts, R. E. Stratmann, O. Yazyev, A. J. Austin, R. Cammi, C. Pomelli, J. W. Ochterski, R. L. Martin, K. Morokuma, V. G. Zakrzewski, G. A. Voth, P. Salvador, J. J. Dannenberg, S. Dapprich, A. D. Daniels, O. Farkas, J. B. Foresman, J. V. Ortiz, J. Cioslowski and D. J. Fox, *Gaussian 09*, Gaussian, Inc., Wallingford CT, 2010.
22 Y. Zhao and D. G. Truhlar, *Theor. Chem. Acc.*, 2008, **120**, 215–241.
23 P. Stephens, F. Devlin, C. Chabalowski and M. J. Frisch, *J. Phys. Chem.*, 1994, **98**, 11623–11627.
24 A. D. Becke, *J. Chem. Phys.*, 1993, **98**, 1372.
25 L. A. Curtiss, P. C. Redfern, K. Raghavachari and J. A. Pople, *J. Chem. Phys.*, 2001, **114**, 108.
26 L. A. Curtiss, P. C. Redfern and K. Raghavachari, *J. Chem. Phys.*, 2007, **126**, 084108.
27 J. MultiWell-2013 Software, designed and maintained by J. R. Barker with contributors N. F. Ortiz, J. M. Preses, L. L. Lohr, A. Maranzana, P. J. Stimac, T. L. Nguyen and T. J. Dhilip Kumar, University of Michigan, Ann Arbor, MI; http://aoss.engin.umich.edu/multiwell/.
28 J. R. Barker, *Int. J. Chem. Kinet.*, 2001, **33**, 232–245.
29 J. R. Barker, *Int. J. Chem. Kinet.*, 2009, **41**, 748–763.
30 A. K. Y. Lam, C. Li, G. Khairallah, B. B. Kirk, S. J. Blanksby, A. J. Trevitt, U. Wille, R. A. J. O'Hair and G. da Silva, *Phys. Chem. Chem. Phys.*, 2012, **14**, 2417–2426.
31 D. M. Golden, *Int. J. Chem. Kinet.*, 2013, **45**, 213–220.
32 H. Durchschlag and P. Zipper, *Ultracentrifugation*, Springer, 1994, pp. 20–39.
33 D. M. Golden, *Int. J. Chem. Kinet.*, 2009, **41**, 573–581.
34 S. J. Blanksby, G. B. Ellison, V. M. Bierbaum and S. Kato, *J. Am. Chem. Soc.*, 2002, **124**, 3196–3197.
35 B. B. Kirk, A. J. Trevitt, B. L. Poad and S. J. Blanksby, *Int. J. Mass Spectrom.*, 2013, **351**, 81–94.
36 G. Gryn'ova, D. L. Marshall, S. J. Blanksby and M. L. Coote, *Nat. Chem.*, 2013, **5**, 474–481.
37 G. Gryn'ova and M. L. Coote, *J. Am. Chem. Soc.*, 2013, **135**, 15392–15403.